INTERNATIONAL JOURNAL OF HYDROGEN ENERGY 45 (2020) 6592–6603

Available online at www.sciencedirect.com

ScienceDirect

journal homepage: www.elsevier.com/locate/he

# A three-dimensional and porous bi-nanospheres electrocatalytic system constructed by in situ generation of Ru nanoclusters inside and outside polydopamine nanoparticles for highly efficient hydrogen evolution reaction

*Jintao Cai* [a,1], *Tao Chen* [a,**,1], *Liang Cui* [b], *Qiang Jia* [a], *Maosheng Liu* [a], *Rongkun Zheng* [b], *Guowen Yan* [a], *Di Wei* [b,***], *Jingquan Liu* [a,b,*]

[a] *College of Materials Science and Engineering; Institute for Graphene Applied Technology Innovation; State Key Laboratory of Biopolysaccharide Fibers and Ecological Textiles, Qingdao University, Qingdao 266071, China*

[b] *College of Material Science and Engineering, Linyi University, Linyi, 276000, China*

## HIGHLIGHTS

- Spherical PDA NPs with controlled sizes from 50 to 500 nm are successfully prepared.
- Ru NCs are generated both inside and outside the porous PDA NPs with electroactive N.
- Both the size of Ru-cPDA NPs and the loading amount of Ru NCs can be well controlled.
- The Ru-cPDA NPs show excellent HER activity and lower cost compared to that of Pt/C.

## GRAPHICAL ABSTRACT

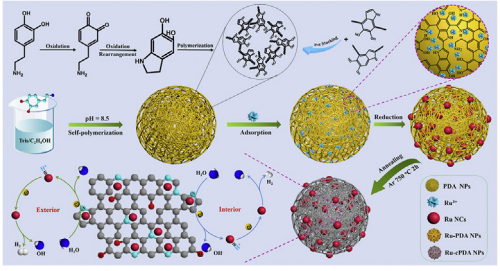


## ARTICLE INFO

*Article history:*
Received 28 October 2019
Received in revised form
23 December 2019
Accepted 2 January 2020
Available online 22 January 2020

## ABSTRACT

Catalytic systems based on nanospheres usually show satisfied catalytic activities due to their huge specific surface areas for active sites immobilization. However, their catalytic activities are usually restricted by the absence of active sites inside the nanospheres and the inadequate communications between the interior and exterior of the nanospheres. Therefore, it can be anticipated that great improvement will be achieved if a porous three-dimensional catalytic system can be designed, through which the activity sites can be distribute interior and exterior. Herein, polydopamine (PDA) NPs with uniform sizes of

* *Corresponding author*.College of Materials Science and Engineering; Institute for Graphene Applied Technology Innovation; State Key Laboratory of Biopolysaccharide Fibers and Ecological Textiles, Qingdao University, Qingdao 266071, China.
** *Corresponding author*.
*** *Corresponding author*.
E-mail addresses: 382388316@qq.com (T. Chen), weidi-cnc@pku.edu.cn (D. Wei), jliu@qdu.edu.cn (J. Liu).
[1] Jintao Cai and Tao Chen contributed equally to this work.
https://doi.org/10.1016/j.ijhydene.2020.01.020

*Keywords:*
Three-dimensional catalytic system
Ru nanoclusters
Omnibearing catalysis
Hydrogen evolution reaction
Porous polydopamine NPs

300 nm are prepared. Then, the Ru nanoclusters (Ru NCs) are uniformly generated inside and on the surface of the PDA NPs to afford the bi-nanospheres (Ru-PDA NPs). After annealing, the porous carbonized Ru-PDA NPs (Ru-cPDA-750 NPs) with electroactive nitrogen atoms are finally obtained, exhibiting small overpotential (42 mV at the current density of 10 mA $cm^{-2}$), low value of Tafel slope (35 mV $decade^{-1}$) and robust stability for hydrogen evolution reaction (HER), which are comparable to that of Pt/C catalyst. Moreover, the study on the effect of Ru NCs amount on electrocatalytic ability reveals that Ru-cPDA NPs loaded with 0.08 wt% of Ru NCs exhibit the best HER catalytic performance compared with the Ru-cPDA NPs loaded with other amount of Ru NCs (0.04–0.16 wt%).



## Introduction

Hydrogen is commonly regarded as the ultimate green energy alternative to fossil energy owing to its renewable and abundant characteristics [1]. An efficient pathway for hydrogen production is to achieve the electrocatalytic splitting of water via hydrogen evolution reaction (HER) [2,3]. Up till now, diverse electrocatalytic systems such as $Mo_2C$ nanoparticles dispersed on carbon microflowers [4], urchin-like $MnO_2$-carbon spheres [5], and Ru nanoclusters (Ru NCs) dispersed on g-$C_3N_4$ nanosheets [6], have been reported and showed satisfied catalytic activity due to their huge specific surface areas for active sites immobilization. However, the active sites were usually distributed on the surface of nanospheres and the huge space inside the nanospheres has not been fully utilized to further enhance catalytic activity. Therefore, it can be anticipated that great improvement will be achieved if all space of nanospheres is fully utilized.

It is imperative to design promising electrocatalysts to trigger proton reduction in minimal overpotential. To date, Pt-group metals, possessing appropriate strength of the Pt–H bond, have been considered as the most active HER electrocatalysts [2,7,8]. However, their scale-up applications are limited by the prohibitive price and scarcity [9–11]. Thus, many studies have been dedicated to explore alternative catalysts with acceptable cost and comparable electrocatalytic activity to replace noble metals. Ru is economically advantageous, and its price is about one-fifteenth of that of Pt. Furthermore, Ru possesses the similar bond strength with hydrogen (~65 kcal $mol^{-1}$) compared with Pt, exhibits good electrocatalytic activity in HER [12], and shows a strong corrosion resistance to the extreme conditions. Although its obvious advantages have been shown in the HER applications, the overpotential and the stability of Ru-based materials need to be further optimized.

It is well-known that nanoparticles in nanoscale usually tend to aggregate to minimize their surface area, resulting in poor performance in electrocatalytic activity and stability [13]. One solution to this obstacle is to apply supporting materials, which are expected not only to enhance the stability of metal nanomaterials, but also greatly improve the catalytic activity. In the past few years, many efforts have been devoted to explore the supporting materials to load Ru-based materials. For instance, Zheng et al. reported that the Ru NPs fixed on g-$C_3N_4$ exhibited satisfied performance in an alkaline solution [14]. Li's group synthesized Ru nanoparticles-modified carbon quantum dots, which showed ideal electrocatalyst for hydrogen production in alkaline condition [15]. Although the HER performance of electrocatalysts have been greatly improved based on the synergistic effect of the employed materials, these electrocatalysts still showed obvious deficiency in stability during electrocatalytic process due to the lack of proper support materials. Therefore, ideal support materials for loading of Ru NCs are still required to construct a robust electrocatalytic system with both good stability and electrocatalytic activity.

Polydopamine (PDA) NPs, as a kind of eco-friendly biomacromolecules prepared by the self-polymerization of dopamine in a facile way, have received increasing attention due to its unique conjugation properties, adhesive ability, and reduction capability [16]. PDA NPs could be directly converted into N-doped conductive carbon materials by heat treatment [17]. More importantly, PDA NPs show strong chelation capability to metal ions and good structural tenability [18], implying the possibility of fabricating many desired nanostructures with adjustable components. Furthermore, PDA NPs possess similar structure and conductivity to multilayer graphene, indicating promising application prospects for fabrication of energy-related devices. Up till now, PDA NPs-derived materials, as nonmetallic heteroatom-doped carbon materials, have been intensively studied for energy related electrocatalytic reactions such as oxygen reduction reaction (ORR) [16,19,20], oxygen evolution reaction (OER) [19,21,22], and HER [22–24] because of their excellent electrical conductivity, tunable molecular structures, abundance, and strong tolerance to acidic/alkaline environments. Therefore, it can be anticipated that their remarkable physicochemical versatility could make PDA NPs highly promising as a simple and effective supporting material to form composites with Ru NCs for the construction of catalytic system with desired HER performance.

Herein, by self-polymerization of dopamine (DA) in alkaline solution (pH = 8.5) at room temperature, PDA NPs were successfully prepared. Ru NCs with average sizes of 4 nm were then uniformly generated inside and on the surface of the obtained PDA NPs to form bi-nanospheres (Ru-PDA NPs) by ultimately in-situ reducing the metal ions chelated with PDA NPs without adding any reductant. Porous carbonized Ru-PDA

NPs (Ru-cPDA NPs) with electroactive nitrogen were finally obtained after annealing. Moreover, both the size of Ru-cPDA NPs and the loading amount of Ru NCs can be controlled and optimized by adjusting the volume ratio of Tris buffer to the ethanol, the content of DA as well as the amount of $RuCl_3$. The resulting samples exhibited a low overpotential (42 mV at the current density of 10 mA $cm^{-2}$), a low value of Tafel slope (35 mV $decade^{-1}$) and robust stability for HER reaction, which were comparable to that of Pt/C catalyst. The three-dimensional (3D) and porous electrocatalytic system provided a powerful platform with omnibearing active sites for the highly effective hydrogen production and guaranteeing the durability during long-term experiment. The synthesized Ru NCs, Ru-PDA NPs and Ru-cPDA NPs were systematically characterized by scanning electron microscopy (SEM), X-ray powder diffraction (XRD) and transmission electron microscope (TEM), to confirm their characteristics and unique properties, accordingly.

## Experimental section

### Materials

Tris(hydroxyethyl)aminomethane (Tris, $C_4H_{11}NO_3$, ≥99.0%), potassium hydroxide (KOH, ≥85.0%), ammonia solution ($NH_3{\cdot}H_2O$, 25.0%–28%) and ethanol absolute ($C_2H_5OH$, ≥99.7%) were obtained from Sinopharm Chemical Reagent Co., Ltd. (Shanghai, China). Dopamine hydrochloride ($C_8H_{11}NO_2{\cdot}HCl$, 98.0%), was bought from Aladdin Industrial Co., Ltd. Ruthenium(III) chloride anhydrous (Ru content 45–55%), was bought from Shanghai Macklin Biochemical Co., Ltd. (Shanghai, China). The commercial Pt/C (10%) was purchased from Alfa Aesar (China) Chemicals Co., Ltd. High purity Ar (99.999%) was bought from Qingdao Heli gas Co., Ltd. (Qingdao, China). All reagents were used as received without further purification.

### Apparatus

High-resolution transmission electron microscopy (HR-TEM) and selected area electron diffraction (SAED) were performed by using a JEM-2100F microscope (JEOL, Japan) operated at a voltage of 200 keV. The morphologies of synthetic materials were characterized by SEM. TEM measurements and Energy dispersive X-ray spectroscopy (EDX) elemental analysis were carried out on a JEM-1200EX transmission electron microscopy operated at an accelerating voltage of 100 kV. Infrared spectra was obtained on a PerkinElmer Spectrum One Fourier transform infrared (FTIR) spectroscope. The crystallographic structures of the materials were analyzed by a powder XRD system (DX-2700, $\lambda = 0.15406$ nm). Raman spectra was taken on confocal Raman microscopy (RM2000, Reinshaw, UK) using He–Ne laser excitation (532 nm). X-ray Photoelectron Spectroscopy (XPS) spectra was collected on Thermo ESCALAB 250 XPS spectrometer using Al Ka X-ray as the excitation source. The $^1H$ NMR spectra were obtained on a JNM-ECP 600 (600 MHz) spectrometer. Inductively coupled plasma-atomic emission spectrometry (ICP-AES) method was employed to determine the Ru loading on cPDA. The specific surface area of materials was determined by the Brunauer-Emmett-Teller (BET) method and the pore size distribution plots were recorded by using Barrett-Joyner-Halenda (BJH) method. The electrochemical tests were measured using a CHI-760D electrochemical workstation (Shanghai, China).

### Preparation of PDA NPs

PDA NPs were prepared according to the previously reported method [25,26]. In details, 144 mL Tris-buffer solution (10 mmol $L^{-1}$, pH = 8.5) was mixed with 64 mL ethanol in a beaker under ambient conditions and stirred for 15 min. 0.04 g of DA hydrochloride was dissolved in deionized water (1 mL) and then added to above solution. Importantly, the polymerization was carried out in air to keep the reaction solution saturated with $O_2$ in solution. After that, the color of solution changed from clear to pale brown owing to the oxidation of DA. After stirring for 30 h, the resulting black suspension was centrifuged at 12,000 rpm, washed using deionized water 3 times, and then dried under vacuum overnight to afford the PDA NPs powder.

### Preparation of Ru-PDA NPs and Ru-cPDA NPs

50 mg of PDA NPs powder was added into 20 mL deionized water, after ultrasonic treatment for 15 min, 10 mL $RuCl_3$ solution (2.2 mmol $L^{-1}$) was added to the above solution, and then stirred for 1.5 h. After that, the mixed solution was adjusted to alkaline (pH = 9) using $NH_3{\cdot}H_2O$ aqueous solution, and it was reacted at room temperature with continuous stirring for 10 h. Next, the resulting black suspension was centrifuged at 10000 rpm, washed with deionized water for 3 times, and then the solid was dried under ambient conditions. Finally, the 10Ru-PDA NPs mixture was obtained ("10" represents the volume of $RuCl_3$ (10 mL) added to the PDA NPs solution, the same was true for 5Ru-PDA NPs, 8Ru-PDA NPs and 20Ru-PDA NPs mentioned below). The Ru-cPDA NPs (named as Ru-cPDA-650 NPs, Ru-cPDA-700 NPs, Ru-cPDA-750 NPs and Ru-cPDA-800 NPs) were obtained after annealing of Ru-cPDA NPs for 2 h under Ar atmosphere at 650 °C, 700 °C, 750 °C, 800 °C, respectively, with a temperature ramping rate of 5 °C·$min^{-1}$.

### Electrochemical tests

The electrochemical measurements were evaluated in a CHI-760D electrochemical workstation, which equipped with conventional three-electrode configuration. The glassy-carbon electrode (GCE, 6 mm diameter, 0.283 $cm^{-2}$) coated with the testing sample was served as working electrode. A graphite rod and a saturated calomel electrode (SCE) were applied as reference and counter electrodes, respectively. The testing sample was fabricated by the following procedure: 5 mg of testing sample (10Ru-cPDA-750 NPs) was dispersed in a solution containing 900 μL water/ethanol ($V_1$: $V_2$ = 1:1) solvent and 30 μL of 5 wt% Nafion solution, followed by ultrasonic mixing for 1 h to generate a uniform catalyst ink. Then 6 μL 10Ru-cPDA-750 NPs was loaded onto the working electrode (0.19 mg $cm^{-2}$ loading amount) which was polished with $Al_2O_3$ powders, and dried at ambient temperature.

All measured potentials were calibrated against the reversible hydrogen electrode (RHE) by the Nernst equation. In 1.0 M KOH, E (RHE) = E (SCE) + 1.068 V. Tafel plots were collected at a scan rate of 5 $mV \cdot s^{-1}$, and the Tafel plots were calculated from the transformation of the polarization curve based on the Tafel equation: $\eta = a + b \log j$, where $\eta$ was overpotential, b was the Tafel slope and j was the current density. All the polarization curves presented were corrected for iR compensation and background current. The commercial Pt/C catalyst (10%, Alfa Aesar) was used as a reference to compare with the electrocatalytic performance of as-prepared samples, cyclic voltammetry (CV) cycles were carried out between 0.97 V and 1.06 V (vs. RHE) at a sweep rate of 50 $mV \cdot s^{-1}$ for 250,000 cycles to investigate the cycling stability.

## Results and discussion

### *Characterizations of the stepwise prepared PDA NPs, Ru-PDA NPs and Ru-cPDA NPs*

A schematic diagram illustrating the preparation process of PDA NPs, Ru-PDA NPs and Ru-cPDA NPs is shown in Fig. 1. In details, PDA NPs could be obtained by spontaneous self-polymerization of DA in weakly alkaline solution (pH = 8.5, Tris solution) of water and ethanol. PDA NPs possessed strong chelating capability with various ions such as $Fe^{3+}$, $Cu^{2+}$, $Ru^{3+}$, owing to the widespread catechol and amino functional groups from DA. Therefore, when $RuCl_3$ was added to the solution of PDA NPs, then large amount of $Ru^{3+}$ could be coordinated by PDA NPs due to the strong chelating capability. Next, the chelated $Ru^{3+}$ ions were further reduced to form Ru NCs via the catechol functional groups on PDA NPs under alkaline conditions. Thus, Ru NCs could be successfully impregnated into or anchored on PDA NPs to obtain Ru-PDA NPs. To ensure the crystallization and electrical conductivity of the materials for better HER performance, the as-prepared Ru-PDA NPs were then annealed at 750 °C for 2 h to obtain Ru-cPDA-750 NPs. The successful preparation of PDA NPs, Ru-PDA NPs and Ru-cPDA NPs was confirmed by systematical characterizations in both physical and chemical structures using SEM, TEM, HRTEM, FTIR, XRD, and XPS, respectively.

*Characterizations of the physical structures of PDA NPs, Ru-PDA NPs and Ru-cPDA NPs*

The morphologies and structures of as-prepared samples were examined by SEM and TEM firstly. Fig. 2A shows that the as-prepared spherical PDA NPs have the uniform size of 300 nm, which can be further confirmed by the TEM image as shown in Fig. 2D. The size and shape of the PDA NPs could be well controlled by adjusting the ratio of tris-buffer to DA, and thus PDA NPs with different sizes in the range from 50 nm to 500 nm were also prepared as shown in Fig. S1. After in situ reduction reaction, a larger number of Ru NCs with the average sizes of 4 nm could be generated on the surface of PDA NPs as evidenced by TEM images (Fig. 2E) which is consistent with the observation from SEM images (Fig. 2B), indicating the Ru NCs have been successfully prepared either inside and on the surface of PDA NPs. After carbonization at 750 °C for 2 h, the shrunken Ru-cPDA NPs with small sizes (200 nm) and concavo-convex micromorphologies could be observed as shown in Fig. 2C. More importantly, Ru NCs were still maintained on PDA NPs after carbonization (Fig. 2F). The concavo-convex micromorphologies further increased the specific surface area of the Ru-cPDA NPs, which could provide a robust platform with much more active sites for the following catalytic reaction. Besides, the specific surface area of the Ru-cPDA-750 NPs was tested using the BET method and the results are shown in Fig. S2. It was revealed that the as-prepared Ru-cPDA-750 NPs exhibited a specific surface area of 565.6 $m^2 \cdot g^{-1}$ with a pore volume of 0.605 $cm^3 \cdot g^{-1}$ and an average pore diameter of 1.21 nm. Hence, the micropores formed during the carbonization process could be benefit for the fast transfer of electron/ion, thereby improving the efficiency of the catalyst. All in all, the high specific surface area and porous structure of Ru-cPDA NPs could provide abundant active sites for HER reaction and benefit for the gas–liquid transfer during the HER process.

*Characterizations of the chemical structures of PDA NPs, Ru-PDA NPs and Ru-cPDA NPs*

In addition to the physical structure, the chemical structures of the samples were also characterized by various characterization methods. EDX elemental analysis (Fig. 2G) under TEM further revealed the coexistence and homogeneous distribution of C, N, O, Ru in Ru-cPDA NPs samples, which evidenced the successfully construction of bi-nanospheres with N-doped and Ru NCs-generated structures. Moreover a representative HRTEM image (Fig. 2H) have also been obtained from the edge of Ru-cPDA NPs. The obvious lattice fringes with an interplanar spacing of 0.213 nm and 0.228 nm, could be attributed to the (100) and (101) plane of Ru NCs, respectively, indicating the high crystallinity of Ru NCs. The polycrystalline nature of the Ru NCs was further examined by the SAED pattern (Fig. 2I), where distinct crystalline Ru-cPDA NPs could be observed from the diffraction spots of (100), (002), (101), (110) and (112), respectively.

More insights into the crystallinity and structures of Ru-cPDA NPs were further studied using XRD. As indicated in Fig. 3A, a typical "bread" peak centered at $2\theta = 26°$ could be observed in all samples, which belonged to the characteristic peak of PDA NPs [27]. The XRD patterns of Ru-cPDA NPs showed a series of peaks at $2\theta = 38°$, 42°, 44°, 58°, 69°, 78°, 84°, and 86°, corresponding to (100), (002), (101), (102), (110), (103), (112), and (201) planes of hexagonal close-packed (hcp) phase of Ru NCs, respectively, which were well consistent with those from the JCPDS NO. 06-0663 [28].

The successful synthesis of PDA NPs was also manifested by FTIR and $^1H$ NMR spectra. As shown in Fig. 3B, the as-prepared samples were characterized by FTIR, the broad peaks around 3000–3400 $cm^{-1}$ could be assigned to the intermolecular hydrogen bonds of DA and aromatic O–H asymmetry stretching vibration [29]. The peaks at 2429 $cm^{-1}$, 2531 $cm^{-1}$, 2634 $cm^{-1}$ and 2746 $cm^{-1}$ are consistent with $-NH_2$ peaks of DA. After self-polymerization, these peaks disappeared because the $-NH_2$ groups have been converted into the secondary amine [30]. Besides, in the FTIR spectra of synthesized PDA NPs, a strong peak at 3429 $cm^{-1}$ should be attributed to the N–H and O–H asymmetry stretching vibration of catechol groups [31,32]. The peaks at 2920 $cm^{-1}$ and

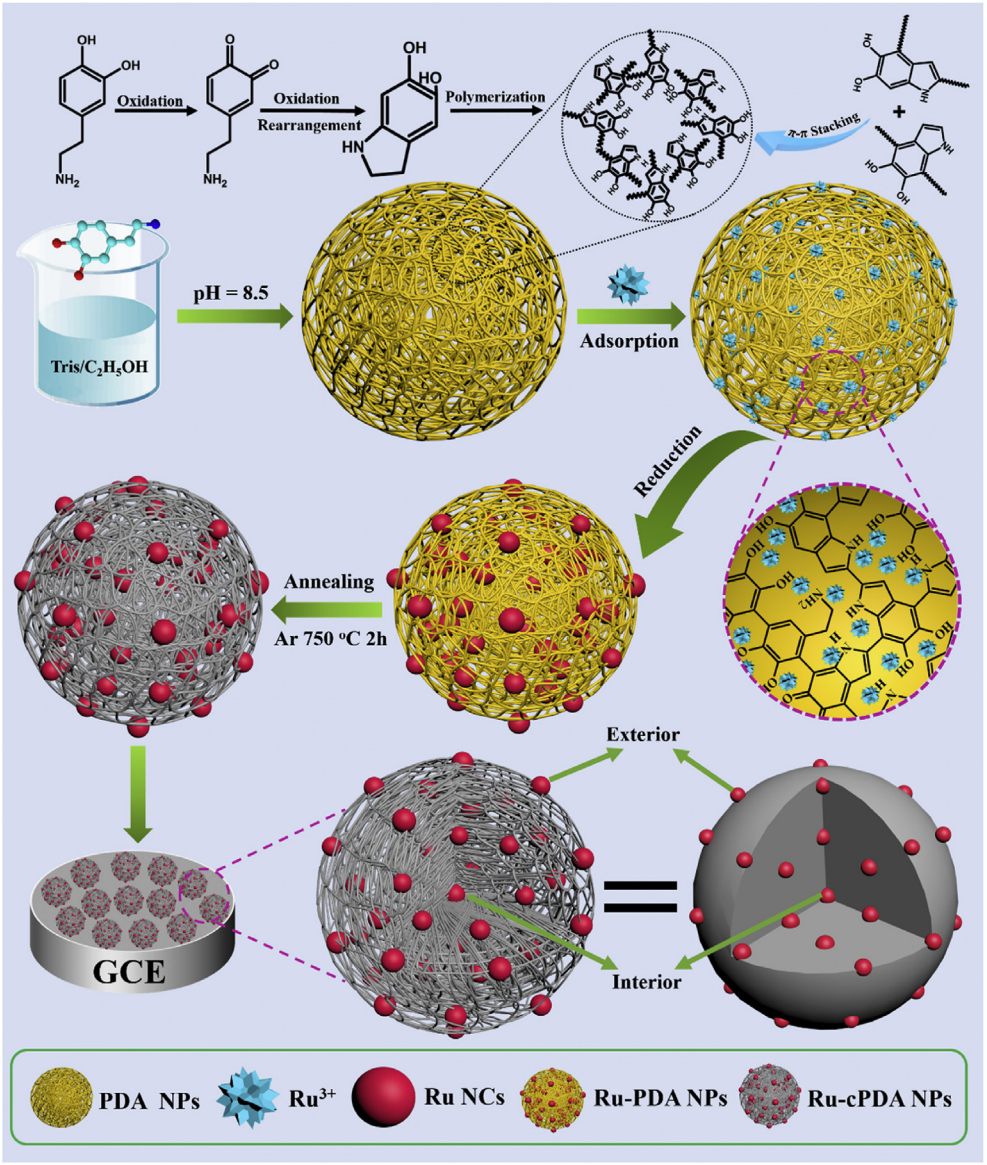


**Fig. 1 – Schematic illustration for the synthetic process of PDA NPs, Ru-PDA NPs and Ru-cPDA NPs, and the porous electrocatalytic system based on Ru-cPDA NPs with impregnated and surface anchored Ru NCs for highly efficient hydrogen evolution reaction in alkaline solution.**

2848 $cm^{-1}$ are correlated with the stretching vibration of $-CH_2$ group. Furthermore, a weaker peak at 1384 $cm^{-1}$ (the stretching vibration of $-CH_3$ group) could be observed, indicating that the as-prepared samples only contained tiny amounts of $sp^3$ C. The characteristic peaks at 1623 $cm^{-1}$ and 1274 $cm^{-1}$ belonged to the vibrational stretching of C=C or C=N in aromatic rings and C–O, respectively. Furthermore, the weak peaks at 1120 $cm^{-1}$ and 1044 $cm^{-1}$ indicated the existence of C–O–C functionality, which might be resulted from the dehydration of the catechol groups on adjacent PDA NPs [33]. The FTIR spectra of Ru-PDA NPs showed that the peak at 1120 $cm^{-1}$ almost disappeared due to the interaction between Ru NCs and PDA NPs. The successful synthesis of PDA NPs was also confirmed by $^1H$ NMR spectra. As shown in Fig. 3C, the apparent peak signals at 6.80–6.50 ppm should be correspond to the aromatic protons in DA, and the peaks at 2.70 and 3.10 ppm should be attributed to the two methylene groups. From Fig. 3D, the obvious decrease of the signal at 6.80–6.50 ppm belonging to aromatic protons could be seen compared with that of DA. This was because that the aromatic rings of DA were broken during the self-polymerization process, further proving the successful synthesis of PDA NPs.

The structure of Ru-cPDA NPs annealed at different temperature was further investigated by Raman spectra, two characteristic peaks, which were corresponding to the well-known D-band (at 1353 $cm^{-1}$) and G-band (at 1587 $cm^{-1}$) of carbon materials, could be distinctly observed in all samples (Fig. 4A). The D band is correlated with the degree of disorder and defectiveness in the structure, while the G band reflects the graphitic degree [34,35]. Accordingly, the graphitization degree of samples could be demonstrated by the D/G ratio of band intensities ($I_D/I_G$). The intensity ratios ($I_D/I_G$) were about

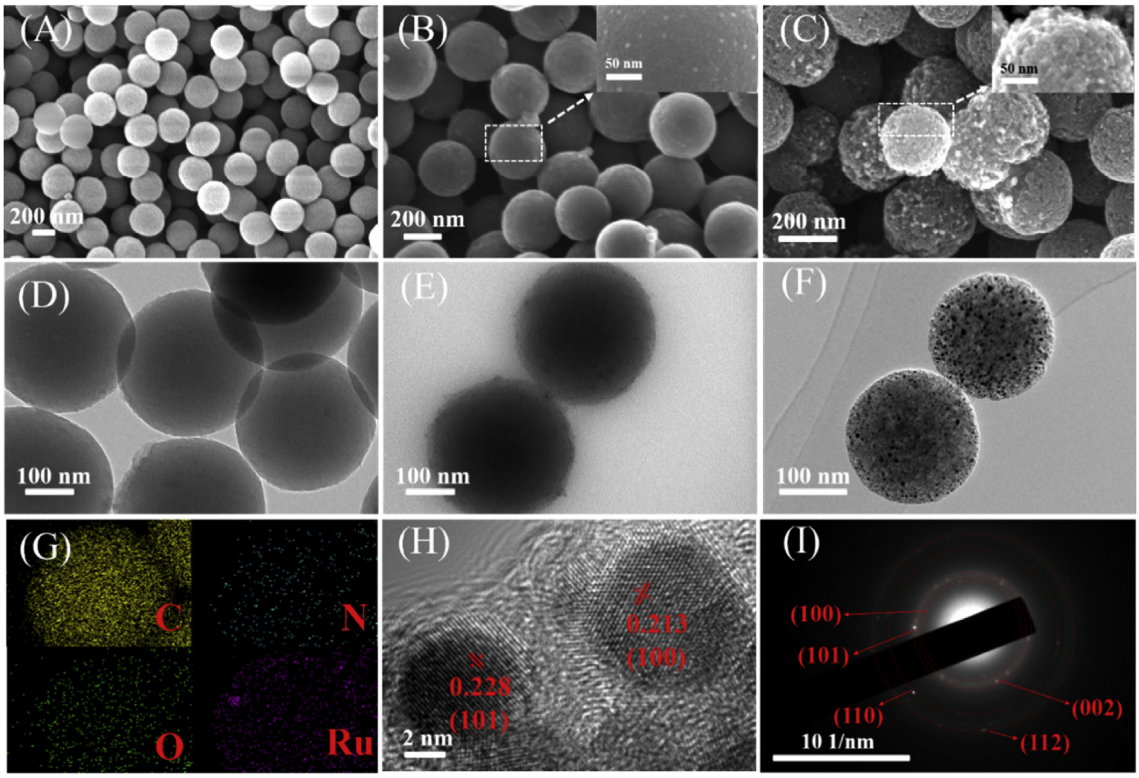


**Fig. 2 – SEM images of (A) PDA NPs, (B) Ru-PDA NPs and (C) Ru-cPDA-750 NPs. TEM images of (D) PDA NPs, (E) Ru-PDA NPs and (F) Ru-cPDA-750 NPs. (G) EDS elemental mapping images for C, N, O, and Ru of Ru-cPDA NPs. (H) HRTEM image of Ru-cPDA NPs, (C) and the corresponding SAED.**

0.98 for Ru-cPDA-650 NPs, 1.01 for Ru-cPDA-700 NPs, 1.04 for Ru-cPDA-750 NPs and 1.05 for Ru-cPDA-800 NPs. The increase of $I_D/I_G$ ratio might result from the more amorphization than graphitization when the annealing temperature increased from 650 to 800 °C. This phenomenon was also observed by other researchers [17,36].

XPS analysis was performed to understand the detailed elemental composition and surface chemical states of the as-prepared PDA NPs, cPDA NPs, and Ru-cPDA NPs. The XPS results of PDA NPs confirmed the presence of C, N, and O elements (Fig. S3A). As exhibited in Fig. S3B, the high-resolution spectrum of C 1s should be fitted into four sub-peaks at 284.10 eV for C–C, 285.45 eV for C–N, 286.51 eV for C–OH of catechol and 290.53 eV for $\pi \rightarrow \pi^*$ which is a typical shake-up feature of aromatic carbon species [37,38]. Similarly, Fig. S3C shows the high-resolution spectrum of N 1s which could be fitted with three main sub-peaks at 401.63 eV, 399.90 eV, and 398.48 eV, corresponding to primary amine (R–$NH_2$), secondary amine (R–NH–R), and aromatic (=N-R) amine, respectively [39], where primary amine should result from the structure of DA. The O 1s spectrum of the XPS (Fig. S3D) could be deconvoluted into two peaks at 530.80 eV for C=O and 532.70 eV for C–O. After carbonization, the as-generated cPDA NPs were also characterized by XPS. As shown in Fig. S4 and Table S1 an increase in C content and a salient loss in O content were observed which should result from the dehydration process in carbonization process. In addition, the bonding configurations of carbon and oxygen remained unchanged compared with that of PDA NPs. Nevertheless, the N 1s spectrum of the XPS demonstrated that the three bonding configurations of N were formed after carbonization, where the peaks at 398.51 eV, 400.60 eV and 401.30 eV can be assigned to the pyridinic N, pyrrolic N and for graphitic N, respectively. As shown in Fig. 4B, the Ru-cPDA NPs were analyzed through XPS, the new peaks for Ru 3d and Ru 3p could be distinctly observed in the survey scans, where the Ru 3d peak at ~280.45 eV overlapped with C 1s peak in the region of 280–290 eV (Fig. 4C). Accordingly, the Ru 3p narrow spectrum was obtained to study the electronic states of Ru. As shown in Fig. 4D, the Ru 3p core-level spectrum was composed of Ru $3p_{3/2}$ and Ru $3p_{1/2}$. The two main spectra could be deconvoluted into four sub-peaks, where the picks at 464.92 eV and 486.13 eV could be interpreted as Ru in metallic state (Ru (0)), whiles the picks at 464.92 eV and 486.13 eV were resulted from the higher valence state of Ru (Ru (IV)) [40]. The presence of Ru (IV) in the results obtained by XPS might be attributed to the following factors. The external factors might come from ruthenium precursors ($RuCl_3$), which might be a mixture of Ru(III) and Ru(IV) instead of pure Ru(III) [38]. On the other hand, it was also possible that Ru NCs were oxidized to $RuO_2$ $xH_2O$ or $RuO_xH_y$ by oxygen in air or solution during XPS sample treatment [38,41,42]. The XPS spectra for the O 1s in Ru-cPDA NPs showed similar features to the O 1s in the cPDA NPs, the only difference was that the peaks at 533.09 eV not only revealed the presence of C–O, but also associated with the interaction between Ru and O (Fig. 4E) [43]. Likewise, as for XPS N 1s spectrum in Fig. 4F, there was no obvious difference compared with that of cPDA NPs, the predominant forms of N

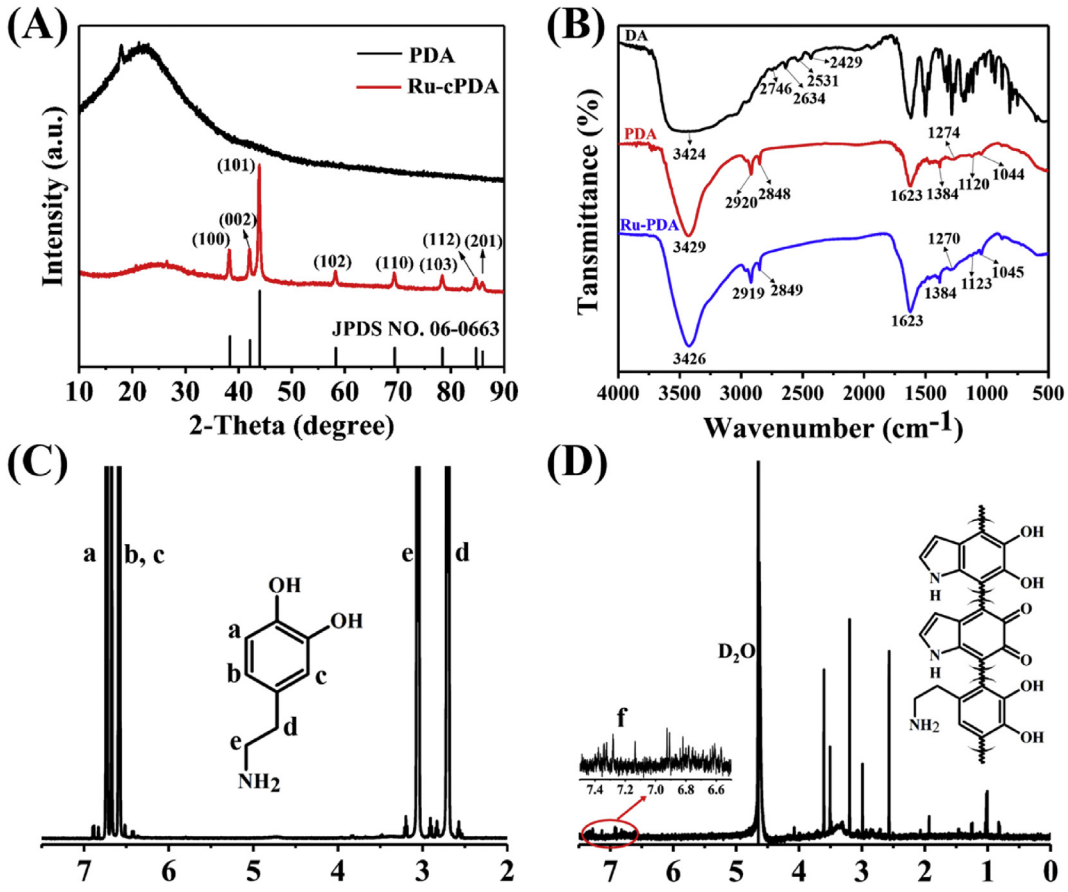


Fig. 3 – (A) XRD pattern of PDA NPs and Ru-cPDA NPs. (B) The FTIR spectra of DA, PDA NPs and Ru-PDA NPs. The $^{1}H$ NMR spectra of the DA (C) and as-prepared PDA NPs (D).

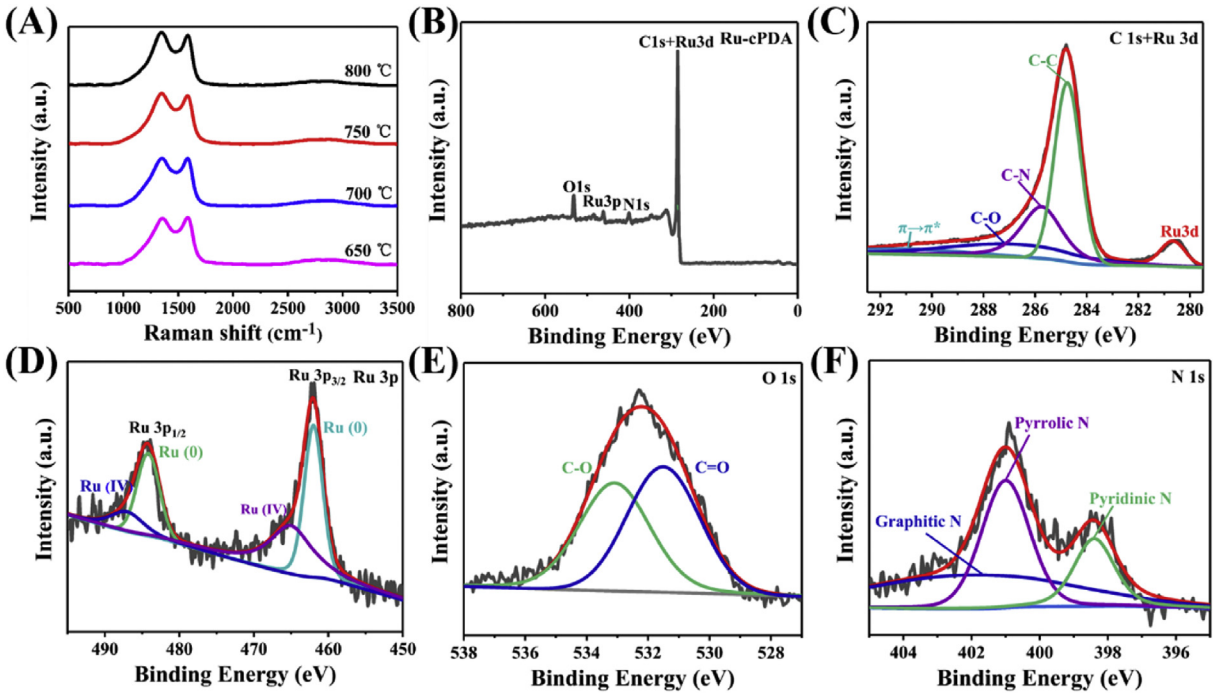


Fig. 4 – (A) The Raman spectra of Ru-cPDA NPs obtained by annealing at different temperatures. (B) XPS survey spectra of Ru-cPDA NPs, and high resolution XPS. (C) C 1s and Ru 3d, (D) Ru 3p, (E) O 1s, (F) N 1s spectra of Ru-cPDA NPs.

were pyridine N and pyrrole N, in addition to a small amount of graphite N. Based on above characterization and those previously reported from the literatures [16,17,21,44], it was doubtless that PDA NPs and Ru-cPDA NPs with expected structures have been successfully prepared. The possible chemical structures of PDA NPs and cPDA NPs had been proposed in Fig. S5.

### *The HER mechanism and performance of the constructed electrocatalytic system based on Ru-cPDA NPs*

#### *The HER mechanism of Ru-cPDA NPs for enhanced HER performance*

In order to understand the reaction mechanisms in alkaline solutions, the possible rate-controlling steps should be discerned from the Tafel slope value derived from the HER polarization curve. The HER electrocatalytic activity of as-prepared Ru-cPDA NPs was evaluated in an alkaline electrolyte (1 M KOH) employing 10 wt% Pt/C as the control experiment under the same condition. The HER electrocatalytic activities of Ru-cPDA NPs constructed by PDA NPs with different diameters (50,100, 200, 300,400, 500 nm) were firstly carried out, respectively. It could be found that the sizes of cPDA NPs had slight influence on HER performance via the comparation of the HER polarization curves and Tafel slopes of these samples (Figs. S6A and 6B). Impressively, the Ru-cPDA NPs prepared by PDA NPs with size of 300 nm showed the best HER performance among the six samples. Therefore, PDA NPs with size of 300 nm were used to construct the Ru-cPDA NPs in the following HER performance. In addition, the low value of Tafel slope (35 $mV \cdot dec^{-1}$) indicated that the HER pathway might be based on Volmer-Heyrovsky HER mechanism [45–47]. According to the Volmer-Heyrovsky HER mechanism in alkaline solution [48,49], the generation process of gaseous hydrogen based on our constructed electrocatalytic system is illustrated in Fig. 5. As shown in Fig. 5A, a 3D catalytic system using porous PDA NPs as the framework to load Ru NCs either inside or on their surface provided a powerful platform for all-around generation of hydrogen. The detailed HER mechanism can be described as follows.

The first step is electrochemical hydrogen adsorption (Volmer reaction) via the following equation: $H_2O + Ru + e^- \rightarrow Ru{-}H^* + OH^-$, forming the Ru–H* bond. And then Ru–H* may experience the electrochemical desorption (Heyrovsky reaction), $Ru{-}H^* + H_2O + e^- \rightarrow Ru + OH^- + H_2$. The interior microstructure of the Ru-cPDA NPs is shown in Fig. 5B, where the Ru NCs are effectively anchored on the skeleton of N-doped PDA NPs and surrounded by three N bonding configurations which are graphitic N, pyrrolic N, and pyridinic N, respectively. The charge density redistribution, resulting from the interiorly doped Ru NCs, drives the electrons transfer from the conductive Ru NCs to cPDA NPs, resulting in the electron-enrichment on the cPDA NPs and hole-enrichment on the Ru NCs. In alkaline HER, $H_2O$ will be adsorbed on the surface of the Ru NCs, and then the adsorbed $H_2O$ is dissociated into H and OH to afford the proton source [12], ultimately produces the intermediate Ru–H*. In this case, the strong attraction to $H_2O$ will promote the $H_2O$ capture rate of Ru clusters, and thus expediting the production of Ru–H*. Concomitantly, the Ru–H* bond is broken and gaseous $H_2$ released. It is worth noting that the doped N atoms can lower the dissociation energy [15], and thus easily accelerating the generation of Ru–H*. Therefore, the interiorly generated Ru NCs will further increase the HER performance. Moreover, the HER polarization curves and Tafel plots provide strong evidence for a collaborative effect between Ru and cPDA NPs to facilitate $H_2O$ adsorption and dissociation, resulting in excellent HER activity of Ru-cPDA NPs.

#### *The optimization of HER performance of Ru-cPDA NPs*

Firstly, the cPDA NPs loaded with different amount of Ru NCs were successfully prepared by adjusting the amount of $RuCl_3$ added to the solution in the preparation process. Their morphologies and proposed structures are shown in Fig. S7, Fig. 5A, C and 5D, respectively. Moreover, their HER performances were also tested and the results are exhibited in Fig. 6A and B. It could be observed that 10Ru-cPDA NPs with an appropriate loading amount (0.08 wt%) of Ru exhibited an optimal HER performance, which can be explained by the most uniform dispersion of abundant Ru NCs on 10Ru-cPDA-750 NPs compared with other samples (Figs. S7A–7D). Too few Ru NCs could not provide enough active sits for the HER reaction and (Fig. 5C, Figs. S7A and 7B), whereas excessive loading amount could result in the aggregation of Ru NCs in the carbonization process (Fig. 5D and Fig. S7D), leading to the hiding of the active sites and consequently decreased catalytic activity.

The HER performances of 10Ru-cPDA NPs annealed at various temperatures were then assayed and the results are shown in Fig. 6C and D. It could be observed that the HER performance of samples enhanced appreciably with the increased annealing temperature from 600 °C to 750 °C, which should be mainly due to the improvement of crystallinity of Ru NCs with the increased annealing temperature (Figs. S8A–8C) [28]. Impressively, the Ru-cPDA NPs showed the best HER performance when the temperature was 750 °C. Continually increasing temperature (800 °C) did no benefit for the enhancement of HER performance because of the melt among Ru NCs as shown in Fig. S8D. In the meanwhile, electrochemical impedance spectroscopy (EIS) was also tested for the 10Ru-cPDA NPs sample annealed at different temperatures (Fig. 6E). It is well-known that the semicircle in the low frequency range reflects the charge-transfer resistance ($R_{ct}$), the smaller semicircle represents the faster charge transfer. The Nyquist plots of 10Ru-cPDA-750 NPs showed the smallest diameter of the semicircle, indicating the fastest interfacial electronic transfer kinetics and electron transfer of 10Ru-cPDA-750 NPs than other samples. This is because that 10Ru-cPDA-750 NPs have the optimum chemical structure constructed by PDA NPs and Ru NCs which could reduce the charge-transfer resistance between the Ru NCs and cPDA NPs and accelerate charge transfer among catalytic active sites.

The porous carbonaceous scaffolds (cPDA NPs) for Ru NCs exactly played a critical role in the HER performance, the uniformly dispersed Ru NCs both inside and outside of the 3D scaffolds achieved the all-around HER performance of the as-prepared catalyst. In the meanwhile, the excellent conductivity of scaffolds is conducive to accelerate charge transfer between catalytic active sites. The double-layer capacitance ($C_{dl}$) is usually employed to evaluate the electrochemical

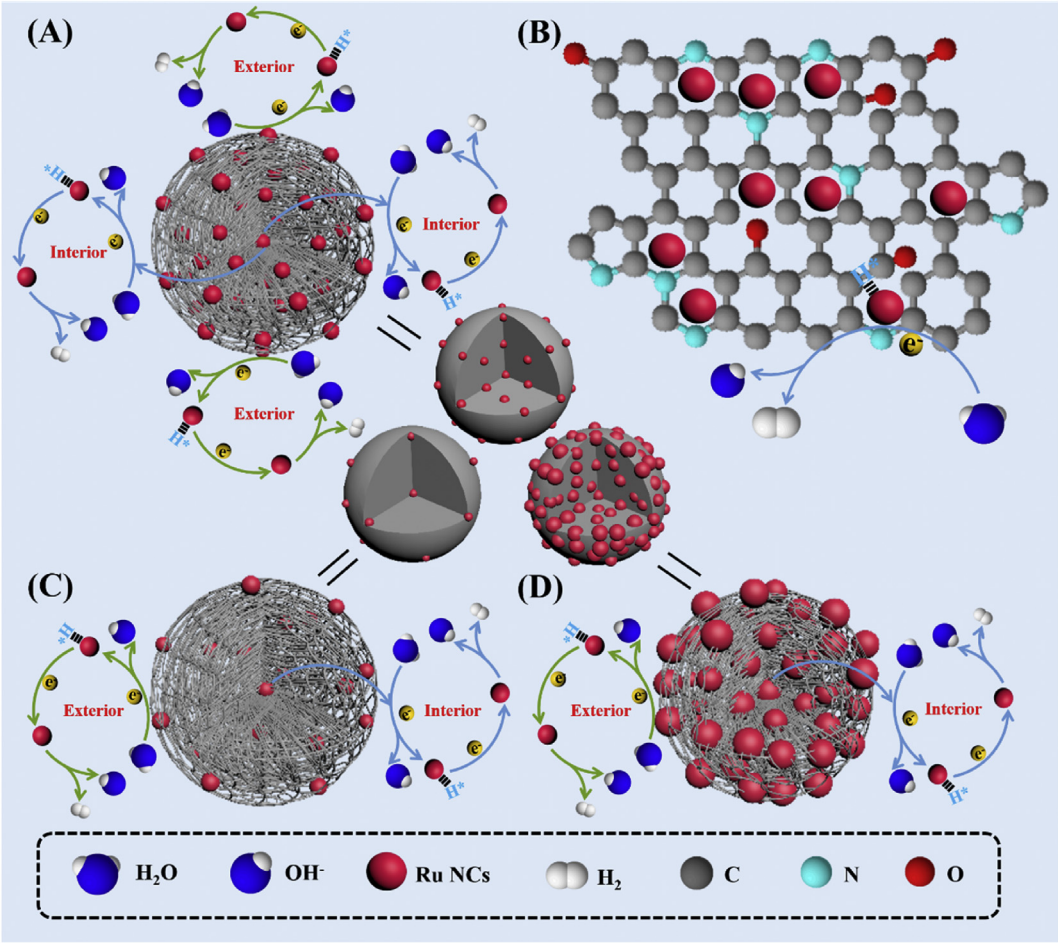


**Fig. 5 – (A) The 3D and porous electrocatalytic system based on bi-nanospheres constructed by interiorly and exteriorly Ru NCs-generated polydopamine for highly efficient hydrogen evolution reaction. (B) The synergistic effect of N-doped PDA and Ru NCs for HER reaction. (C) and (D) are the 3D and porous electrocatalytic system loaded with different amount of Ru NCs.**

active surface area (ECSA) of samples [50]. The $C_{dl}$ of Ru-cPDA-750 NPs was investigated by CV curves at various scan rates of 20–180 $mV \cdot s^{-1}$ between 0.828 and 1.067 V (vs. RHE, a non-Faradaic potential region) (Fig. 6F). Fig. 6G shows the difference between anodic and cathodic current density at the center of potential (0.948 V (vs. RHE)), which exhibits a linear relationship to the various scan rates, in which the slope is equal to the electrochemical $C_{dl}$. The capacitance of Ru-cPDA-750 NPs was 10.3 $mF \cdot cm^{-2}$, then the value of ECSA was calculated to be 67.76 $m^2 \cdot g^{-1}$ according to the standard value of 40 $\mu F \cdot cm^{-2}$ [15,51]. (the calculation details are shown in Method 1 of Supporting Information). In the meanwhile, the samples annealed at other temperatures were also tested by CV cycling (Figs. S9B–9D), and the results showed that the $C_{dl}$ values of Ru-cPDA-650 NPs, Ru-cPDA-700 NPs and Ru-cPDA-800 NPs were derived to be 2.86 $mF \cdot cm^{-2}$, 4.08 $mF \cdot cm^{-2}$ and 6.61 $mF \cdot cm^{-2}$, respectively. It could be observed that Ru-cPDA-750 NPs possessed the largest ESCA and the most active sites, which resulted in the highest HER performance. Moreover, too high annealing temperature (800 °C) could lead to the melt among the Ru NCs, leading to the decreased electrocatalytic activities of the sample (Figs. S8C–8D).

All in all, the as-prepared 10Ru-cPDA-750 NPs exhibited the best HER catalytic performance with the lowest overpotential (42 mV at the current density of 10 mA $cm^{-2}$) and a low value of Tafel slope (35 mV $decade^{-1}$) due to the appropriate amount of loaded Ru NCs and the best crystallinity obtained from the annealing at 750 °C (Fig. S9A). The Tafel slope of 10Ru-cPDA-750 NPs was slightly higher than that of Pt/C (27 mV $decade^{-1}$) and superior to those of Ru-based electrocatalysts recently reported (Table S2). More significantly, the content of loaded Ru in 10Ru-cPDA-750 NPs was only 0.08 wt% (obtained by ICP-AES analysis), which was much lower than the Pt content (10 wt%) in Pt/C catalyst, indicating that the 10Ru-cPDA-750 NPs could be an efficient catalyst with much lower cost and comparable HER performance compared with Pt/C catalyst.

### *Anti-toxicity experiment and long-term stability*

In order to achieve more comprehensive understanding of the active sites on the constructed catalytic system, anti-toxicity experiment has been also carried out by introducing $SCN^-$ (10 mmol) into alkaline electrolyte, which is usually identified as the poisoner of metal-centered active sites. Current-time

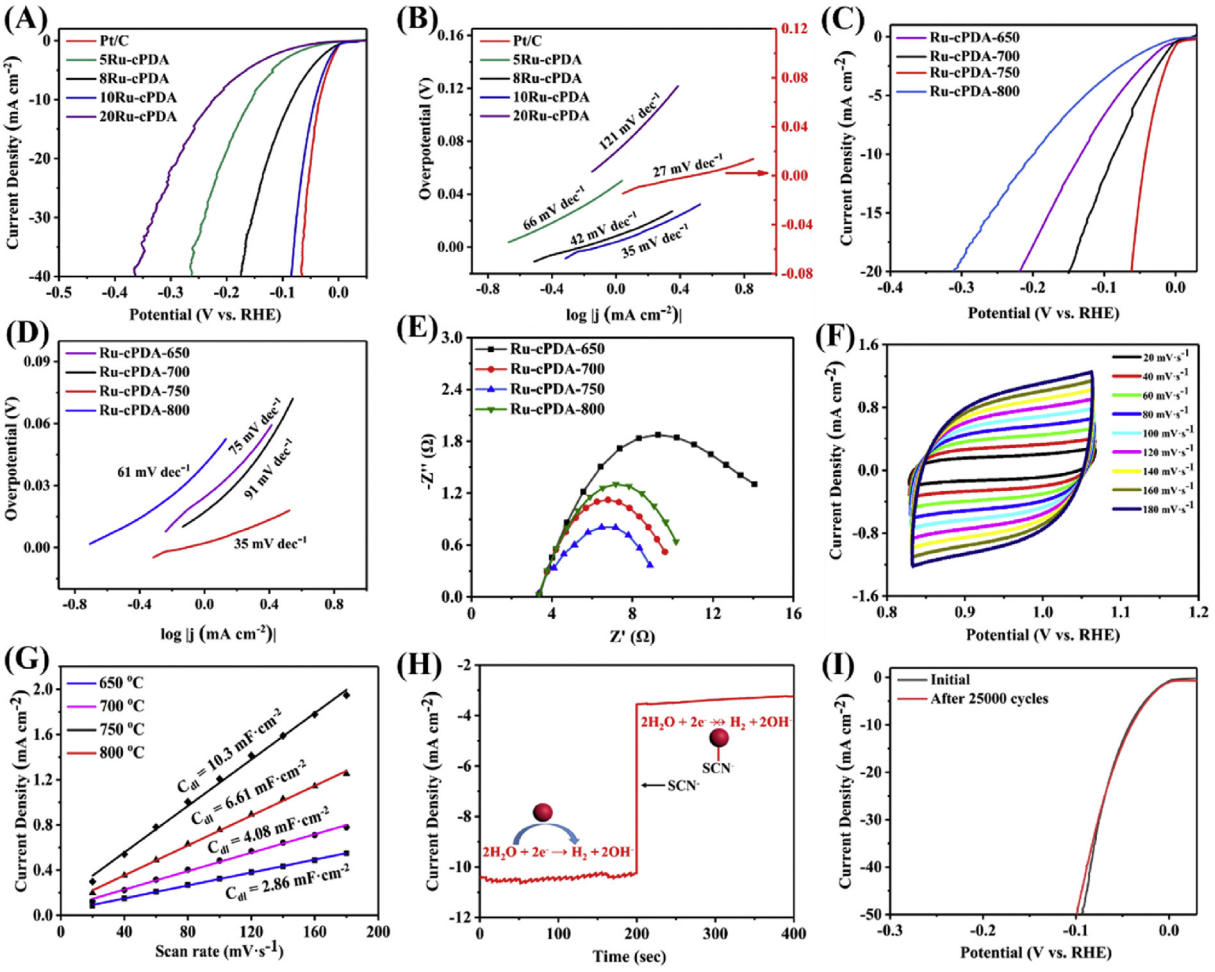


**Fig. 6 – (A)The HER polarization curves at 5 mV·s$^{-1}$ in 1 M KOH for Ru-cPDA-750 NPs with different loading amount of Ru NCs and 10 wt% Pt/C catalyst. (B) The corresponding Tafel plots recorded on glassy carbon electrodes with samples loading of 0.19 mg·cm$^{-2}$. (C) HER polarization curves for the 10Ru-cPDA NPs annealed at various temperatures, and (D) the corresponding Tafel plots. (E) Nyquist plots for the 10Ru-cPDA NPs annealed at different temperature. (F) CV curves of 10Ru-cPDA-750 NPs at various scan rates of 20–180 mV·s$^{-1}$ between 0.828 and 1.067 V (vs. RHE, a non-Faradaic potential region) (G) The plot of capacitive currents at 0.948 V (vs. RHE) against the scan rate. (H) Current-time curve of Ru-cPDA NPs before and after the addition of SCN$^-$ ions in 1 M KOH solution. (I) Polarization curves of Ru-cPDA NPs before and after 25,000 CV cycles between 0.97 V and 1.06 V (vs. RHE) at 50 mV·s$^{-1}$ in alkaline solution.**

curves of the 10Ru-cPDA-750 NPs have been collected before and after the addition of SCN$^-$ in 1 M KOH solution (Fig. 6H). The active sites of Ru NCs were available for proton adsorption from $H_2O$ desorption and the release of $H_2$ without SCN$^-$. Interestingly, the HER current of 10Ru-cPDA-750 NPs decreased suddenly after the addition of SCN$^-$ at 200s, revealing the inactivation of active sites because the Ru NCs were binded by SCN$^-$, further confirming that the Ru NCs was truly the active sites of the Ru-cPDA NPs catalyst [15].

Long-term stability of catalysts is a significant factor to assess for practical applications. The electrochemical stability of Ru-cPDA NPs in alkaline electrolytes was continuously studied. To investigate the cycling stability, the working electrode was continuously tested for 25,000 CV cycles between 0.97 V and 1.06 V (vs. RHE) at 50 mV·s$^{-1}$ in alkaline solution, and the polarization curves were periodically collected. The polarization curves before and after 25,000 cycles almost overlapped with each other (Fig. 6I), demonstrating the good stability of the as-prepared Ru-cPDA NPs.

## Conclusion

In summary, PDA NPs with uniform sizes were prepared by the self-polymerization of DA, then applied as a porous and nontoxic scaffold for the immobilization of Ru NCs inside and outside. The obtained Ru-PDA NPs were carbonized at 750 °C to obtain a 3D electrocatalytic system (Ru-cPDA NPs) with electroactive nitrogen atoms, which provided an electrocatalytic system with omnibearing active sites for the highly effective hydrogen production. In details, the resulting samples (10Ru-cPDA-750 NPs) for HER reaction exhibited the lowest overpotential (42 mV at the current density of 10 mA cm$^{-2}$), a low value of Tafel slope (35 mV decade$^{-1}$) and

robust stability towards a cyclic voltammetry for more than 25,000 cycles, which were comparable to that of Pt/C catalyst. More significantly, the content of loaded Ru in 10Ru-cPDA-750 NPs was only 0.08 wt%, which was much lower than the Pt content (10 wt%) in Pt/C catalyst, indicating that the 10Ru-cPDA-750 NPs could be an efficient catalyst for HER compared with Pt/C catalyst. Moreover, this facile and low-cost approach opened a new opportunities for the construction of the porous 3D platform with high specific surface area and abundant active sites, which could be further broadened in potential applications such as sensors, photo-thermal therapy and even supercapacitors.

## Acknowledgements

This work was supported by Qingdao Innovation Leading Talent Program, Qingdao (12-1-4-2-2-jch) and Taishan Scholars Program. National Natural Science Foundation of China (21805124), and Natural Science Foundation of Shandong Province (ZR2018BEM020).

## Appendix A. Supplementary data

Supplementary data to this article can be found online at https://doi.org/10.1016/j.ijhydene.2020.01.020.

## REFERENCES

[1] Turner JA. Sustainable hydrogen production. Science 2004;305:972–4.
[2] Yang J, Chen B, Liu X, Liu W, Li Z, Dong J, Chen W, Yan W, Yao T, Duan X. Efficient and robust hydrogen evolution: phosphorus nitride imide nanotubes as supports for anchoring single ruthenium sites. Angew Chem Int Ed 2018;57:9495–500.
[3] Liu S, Jiang A, Wang Z, Lin M, Xia D, Li Q, et al. Porous coordination polymer-derived ultrasmall CoP encapsulated in nitrogen-doped carbon for efficient hydrogen evolution in both acidic and basic media. Int J Hydrogen Energy 2020;45(3):1729–37.
[4] Huang Y, Gong Q, Song X, Feng K, Nie K, Zhao F, Wang Y, Zeng M, Zhong J, Li Y. Mo2C nanoparticles dispersed on hierarchical carbon microflowers for efficient electrocatalytic hydrogen evolution. ACS Nano 2016;10:11337–43.
[5] Zhang J-H, Feng J-Y, Zhu T, Liu Z-L, Li Q-Y, Chen S-Z, Xu C-W. Pd-doped urchin-like MnO2-carbon sphere three-dimensional (3D) material for oxygen evolution reaction. Electrochim Acta 2016;196:661–9.
[6] Wang J, Wei Z, Mao S, Li H, Wang Y. Highly uniform Ru nanoparticles over N-doped carbon: pH and temperature-universal hydrogen release from water reduction. Energy Environ Sci 2018;11:800–6.
[7] Popczun EJ, Mckone JR, Read CG, Biacchi AJ, Wiltrout AM, Lewis NS, Schaak RE. Nanostructured nickel phosphide as an electrocatalyst for the hydrogen evolution reaction. J Am Chem Soc 2013;135:9267–70.
[8] Sumi V, Meera M, Sha MA, Shibli S. Effect of rGO on Fe2O3–TiO2 composite incorporated NiP coating for boosting hydrogen evolution reaction in alkaline solution. Int J Hydrogen Energy 2020;45(4):2460–77.
[9] Cao B, Veith GM, Neuefeind JC, Adzic RR, Khalifah PG. Mixed close-packed cobalt molybdenum nitrides as non-noble metal electrocatalysts for the hydrogen evolution reaction. J Am Chem Soc 2013;135:19186–92.
[10] Subbaraman R, Tripkovic D, Strmcnik D, Chang K-C, Uchimura M, Paulikas AP, Stamenkovic V, Markovic NM. Enhancing hydrogen evolution activity in water splitting by tailoring Li+-Ni (OH) 2-Pt interfaces. Science 2011;334:1256–60.
[11] Huang L, Ai L, Wang M, Jiang J, Wang S. Hierarchical MoS2 nanosheets integrated Ti3C2 MXenes for electrocatalytic hydrogen evolution. Int J Hydrogen Energy 2019;44:965–76.
[12] Mahmood J, Li F, Jung S-M, Okyay MS, Ahmad I, Kim S-J, Park N, Jeong HY, Baek J-B. An efficient and pH-universal ruthenium-based catalyst for the hydrogen evolution reaction. Nat Nanotechnol 2017;12:441–6.
[13] Du X, He J. Amino-functionalized silica nanoparticles with center-radially hierarchical mesopores as ideal catalyst carriers. Nanoscale 2012;4:852–9.
[14] Zheng Y, Jiao Y, Zhu Y, Li LH, Han Y, Chen Y, Jaroniec M, Qiao SZ. High electrocatalytic hydrogen evolution activity of an anomalous ruthenium catalyst. J Am Chem Soc 2016;138:16174–81.
[15] Li W, Liu Y, Wu M, Feng X, Redfern SA, Shang Y, Yong X, Feng T, Wu K, Liu Z. Carbon-quantum-dots-loaded ruthenium nanoparticles as an efficient electrocatalyst for hydrogen production in alkaline media. Adv Mater 2018;30:1800676.
[16] Ai K, Liu Y, Ruan C, Lu L, Lu G. Sp2 C-dominant N-doped carbon sub-micrometer spheres with a tunable size: a versatile platform for highly efficient oxygen-reduction catalysts. Adv Mater 2013;25:998–1003.
[17] Li H, Aulin YV, Frazer L, Borguet E, Kakodkar R, Feser J, Chen Y, An K, Dikin DA, Ren F. Structure evolution and thermoelectric properties of carbonized polydopamine thin films. ACS Appl Mater Interfaces 2017;9:6655–60.
[18] Ma FX, Wu HB, Xia BY, Xu CY, Lou XW. Hierarchical β-Mo2C nanotubes organized by ultrathin nanosheets as a highly efficient electrocatalyst for hydrogen production. Angew Chem Int Ed 2015;54:15395–9.
[19] Qu K, Zheng Y, Dai S, Qiao SZ. Graphene oxide-polydopamine derived N, S-codoped carbon nanosheets as superior bifunctional electrocatalysts for oxygen reduction and evolution. Nano Energy 2016;19:373–81.
[20] Zhang H, Liu X, He G, Zhang X, Bao S, Hu W. Bioinspired synthesis of nitrogen/sulfur co-doped graphene as an efficient electrocatalyst for oxygen reduction reaction. J Power Sources 2015;279:252–8.
[21] Qu K, Zheng Y, Jiao Y, Zhang X, Dai S, Qiao SZ. Polydopamine-Inspired, dual heteroatom-doped carbon nanotubes for highly efficient overall water splitting. Adv Energy Mater 2017;7:1602068.
[22] Zhang Z, Yi Z, Wang J, Tian X, Xu P, Shi G, Wang S. Nitrogen-enriched polydopamine analogue-derived defect-rich porous carbon as a bifunctional metal-free electrocatalyst for highly efficient overall water splitting. J Mater Chem 2017;5:17064–72.
[23] Qu K, Wang Y, Vasileff A, Jiao Y, Chen H, Zheng Y. Polydopamine-inspired nanomaterials for energy conversion and storage. J Mater Chem 2018;6:21827–46.
[24] Zeng L, Li X, Fan S, Zhang M, Yin Z, Tadé M, Liu S. Photo-driven bioelectrochemical photocathode with polydopamine-coated TiO2 nanotubes for self-sustaining MoS2 synthesis to facilitate hydrogen evolution. J Power Sources 2019;413:310–7.

[25] Liu Y, Ai K, Liu J, Deng M, He Y, Lu L. Dopamine-melanin colloidal nanospheres: an efficient near-infrared photothermal therapeutic agent for in vivo cancer therapy. Adv Mater 2013;25:1353–9.
[26] Liu Y, Ai K, Lu L. Polydopamine and its derivative materials: synthesis and promising applications in energy, environmental, and biomedical fields. Chem Rev 2014;114:5057–115.
[27] Chen T, Xu Y, Wei S, Li A, Huang L, Liu J. A signal amplification system constructed by bi-enzymes and bi-nanospheres for sensitive detection of norepinephrine and miRNA. Biosens Bioelectron 2019;124:224–32.
[28] Li Y, Zhang LA, Qin Y, Chu F, Kong Y, Tao Y, Li Y, Bu Y, Ding D, Liu M. Crystallinity dependence of ruthenium nanocatalyst toward hydrogen evolution reaction. ACS Catal 2018;8:5714–20.
[29] Ghorbani F, Zamanian A, Behnamghader A, Joupari MD. A facile method to synthesize mussel-inspired polydopamine nanospheres as an active template for in situ formation of biomimetic hydroxyapatite. Mater Sci Eng C 2019;94:729–39.
[30] Yu F, Chen S, Chen Y, Li H, Yang L, Chen Y, Yin Y. Experimental and theoretical analysis of polymerization reaction process on the polydopamine membranes and its corrosion protection properties for 304 Stainless Steel. J Mol Struct 2010;982:152–61.
[31] Nishizawa N, Kawamura A, Kohri M, Nakamura Y, Fujii S. Polydopamine particle as a particulate emulsifier. Polymers 2016;8:62. https://doi.org/10.3390/polym8030062.
[32] Luo H, Gu C, Zheng W, Dai F, Wang X, Zheng Z. Facile synthesis of novel size-controlled antibacterial hybrid spheres using silver nanoparticles loaded with poly-dopamine spheres. RSC Adv 2015;5:13470–7.
[33] Li H, Shen L, Yin K, Ji J, Wang J, Wang X, Zhang X. Facile synthesis of N-doped carbon-coated Li 4 Ti 5 O 12 microspheres using polydopamine as a carbon source for high rate lithium ion batteries. J Mater Chem 2013;1:7270–6.
[34] Li Z, Xu Z, Wang H, Ding J, Zahiri B, Holt CM, Tan X, Mitlin D. Colossal pseudocapacitance in a high functionality–high surface area carbon anode doubles the energy of an asymmetric supercapacitor. Energy Environ Sci 2014;7:1708–18.
[35] Li Y, Wang G, Wei T, Fan Z, Yan P. Nitrogen and sulfur co-doped porous carbon nanosheets derived from willow catkin for supercapacitors. Nano Energy 2016;19:165–75.
[36] Pan G, Li B, Heath M, Horsell D, Wears ML, Al Taan L, Awan S. Transfer-free growth of graphene on SiO2 insulator substrate from sputtered carbon and nickel films. Carbon 2013;65:349–58.
[37] Pirlot C, Willems I, Fonseca A, Nagy JB, Delhalle J. Preparation and characterization of carbon nanotube/polyacrylonitrile composites. Adv Eng Mater 2002;4:109–14.
[38] Rojas J, Toro-Gonzalez M, Molina-Higgins M, Castano C. Facile radiolytic synthesis of ruthenium nanoparticles on graphene oxide and carbon nanotubes. Mater Sci Eng, B 2016;205:28–35.
[39] Liu T, Kim KC, Lee B, Chen Z, Noda S, Jang SS, Lee SW. Self-polymerized dopamine as an organic cathode for Li-and Na-ion batteries. Energy Environ Sci 2017;10:205–15.
[40] Zhang Y, Jiang H, Li G, Zhang M. Controlled synthesis of highly dispersed and nano-sized Ru catalysts supported on carbonaceous materials via supercritical fluid deposition. RSC Adv 2016;6:16851–8.
[41] Park KC, Jang IY, Wongwiriyapan W, Morimoto S, Kim YJ, Jung YC, Toya T, Endo M. Carbon-supported Pt–Ru nanoparticles prepared in glyoxylate-reduction system promoting precursor–support interaction. J Mater Chem 2010;20:5345–54.
[42] Edison TNJI, Atchudan R, Lee YR. Facile synthesis of carbon encapsulated RuO2 nanorods for supercapacitor and electrocatalytic hydrogen evolution reaction. Int J Hydrogen Energy 2019;44:2323–9.
[43] Shen J, Adnot A, Kaliaguine S. An ESCA study of the interaction of oxygen with the surface of ruthenium. Appl Surf Sci 1991;51:47–60.
[44] Liebscher Jr, Mrówczynski R, Scheidt HA, Filip C, Hadade ND, Turcu R, Bende A, Beck S. Structure of polydopamine: a never-ending story? Langmuir 2013;29:10539–48.
[45] Bockris JM, Potter E. The mechanism of the cathodic hydrogen evolution reaction. J Electrochem Soc 1952;99:169–86.
[46] Liao L, Wang S, Xiao J, Bian X, Zhang Y, Scanlon MD, Hu X, Tang Y, Liu B, Girault HH. A nanoporous molybdenum carbide nanowire as an electrocatalyst for hydrogen evolution reaction. Energy Environ Sci 2014;7:387–92.
[47] Xiao P, Chen W, Wang X. A review of phosphide-based materials for electrocatalytic hydrogen evolution. Adv Energy Mater 2015;5:1500985.
[48] Zheng Y, Jiao Y, Vasileff A, Qiao SZ. The hydrogen evolution reaction in alkaline solution: from theory, single crystal models, to practical electrocatalysts. Angew Chem Int Ed 2018;57:7568–79.
[49] Strmcnik D, Lopes PP, Genorio B, Stamenkovic VR, Markovic NM. Design principles for hydrogen evolution reaction catalyst materials. Nano Energy 2016;29:29–36.
[50] Zhang H, Yu L, Chen T, Zhou W, Lou XW. Surface modulation of hierarchical MoS2 nanosheets by Ni single atoms for enhanced electrocatalytic hydrogen evolution. Adv Funct Mater 2018;28:1807086.
[51] Hou Y, Liu Y, Gao R, Li Q, Guo H, Goswami A, Zboril R, Gawande MB, Zou X. Ag@ Co x P core–shell heterogeneous nanoparticles as efficient oxygen evolution reaction catalysts. ACS Catal 2017;7:7038–42.